Supplementary Figures

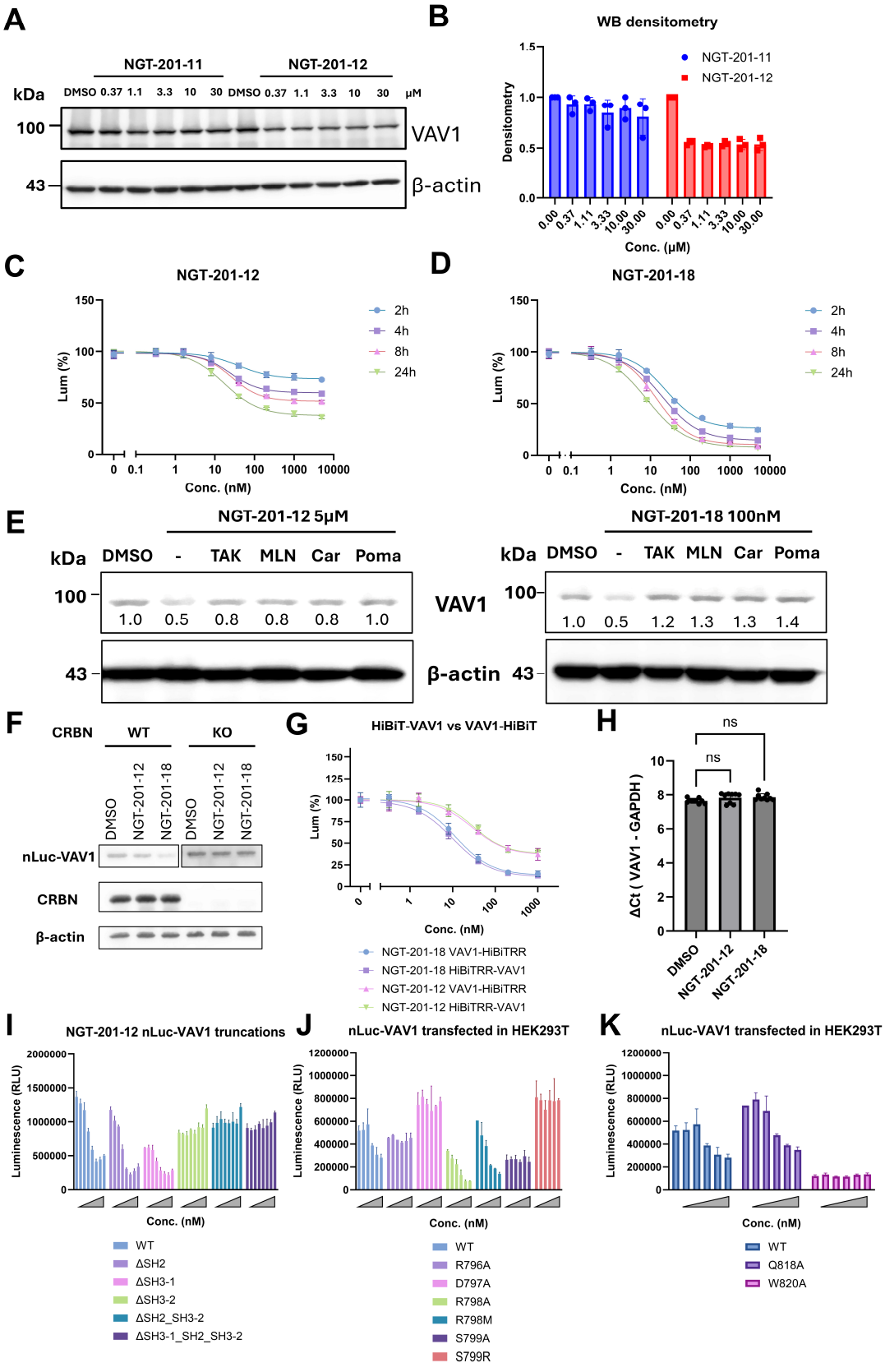

Figure S1. NGT-201-12 and -18 are VAV1 degraders.

(A) Representative Western blot analysis of endogenous VAV1 by 24 hours NGT-201-11 and NGT-201-12 treatment in Jurkat cells. **(B)** Quantitative analysis of panel E western blots with three biological replicates. **(C-D)** Jurkat VAV1-HiBiT KI cell line treated with various concentration of NGT-201-12 (A) or NGT-201-18 (B) for 2, 4, 8, 24h. **(E)** WB analysis of Jurkat WT cell line treated with DMSO, NGT-201-12 5 μM or NGT-201-18 100 nM for 4 h, with 0.5 h pretreat and 4 h co-treatment of TAK-243 (TAK) 1 μM, MLN-4924 (MLN) 1 μM, Carfilzomib (Car) 1 μM, or Pomalidomide (Poma) 20 μM. **(F)** WB analysis of HEK293T cells (WT or CRBN-knockout) transfected with nLuc-VAV1 and treated with 1 μM NGT-201-12 or 18 for 24 h. **(G)** HeLa cells transfected with HiBiTRR-VAV1 or VAV1-HIBITRR and treated with various concentrations of NGT-201-12 or -18 for 24h. **(H)** RT-qPCR of VAV1 mRNA transcript after 24h treatment of DMSO, 1 μM NGT-201-12 or -18 in Jurkat WT cells. **(I)** Raw luminescence readout for Figure 1E. **(J-K)** Raw luminescence readout for Figure 3E.

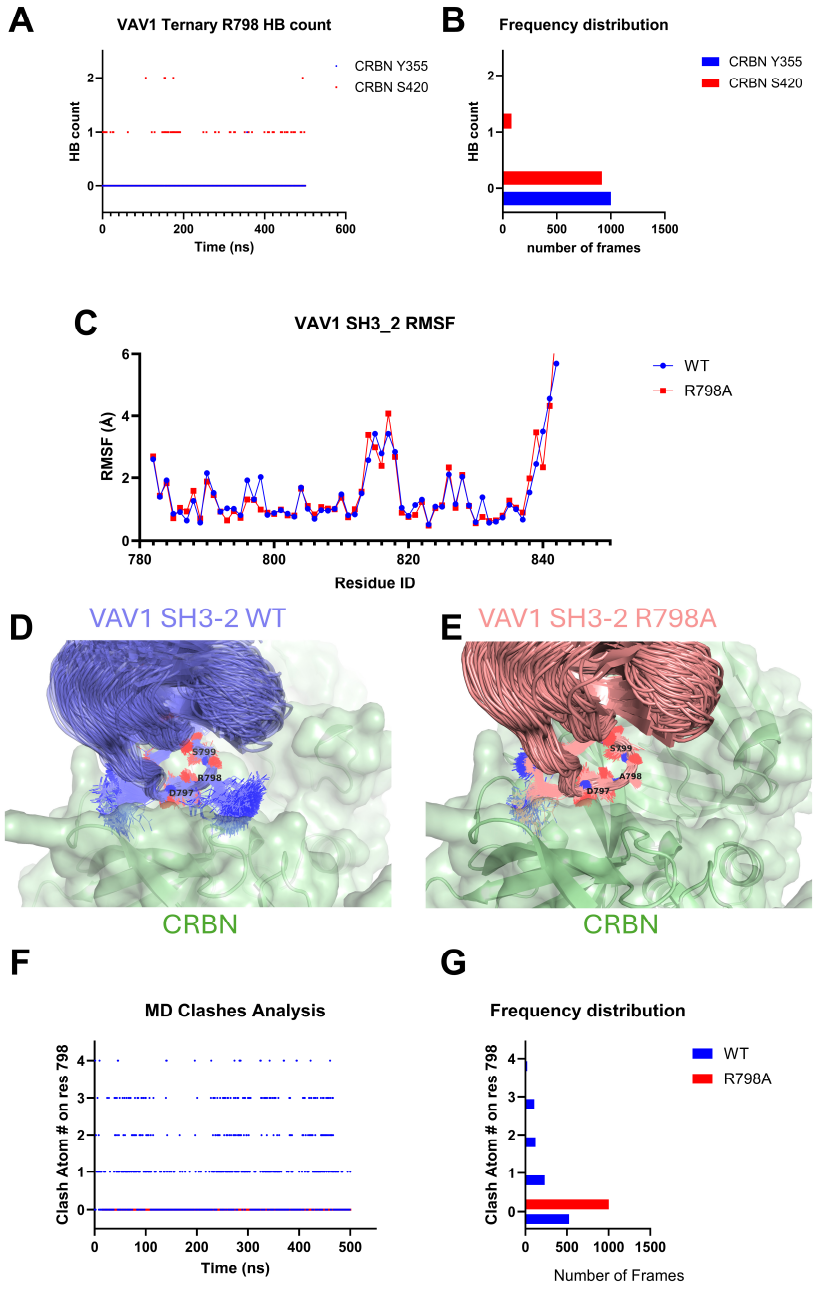

Figure S2. VAV1 R798 is a negative contributor to ternary formation with CRBN.

(A) Hydrogen bond analysis of VAV1 R798 with CRBN Y355/S420 in the 500 ns MD simulation of VAV1:NGT-201-12:CRBN ternary complex. **(B)** Frequency distribution of panel A. **(C)** RMSF of VAV1 SH3-2 domain for WT and R798A mutant during 500ns MD simulation. **(D)** The R798 residue side chain in unbound VAV1 SH3-2 domain will sample various conformations, and some of which forms clashes when aligned to the CRBN:NGT-201-12:VAV1 ternary model. **(E)** The R798A residue side chain in unbound VAV1 SH3-2 domain is stable, avoid forming clashes when aligned to the CRBN:NGT-201-12:VAV1 ternary model. **(F)** Quantification of the clashed atom number on R798 or R798A during the 500 ns MD simulation and **(G)** shows the frequency distribution.

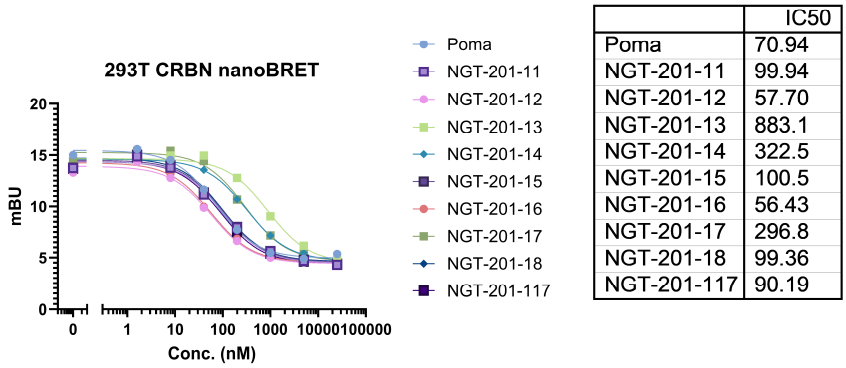

	IC50
Poma	70.94
NGT-201-11	99.94
NGT-201-12	57.70
NGT-201-13	883.1
NGT-201-14	322.5
NGT-201-15	100.5
NGT-201-16	56.43
NGT-201-17	296.8
NGT-201-18	99.36
NGT-201-117	90.19

Figure S3. CRBN NanoBRET target engagement assay in HEK293T cells using 500 nM CRBN tracer.

Tracer was balanced for 1h before 2h incubation of degraders. Data are presented as mean ± SD from three independent experiments.

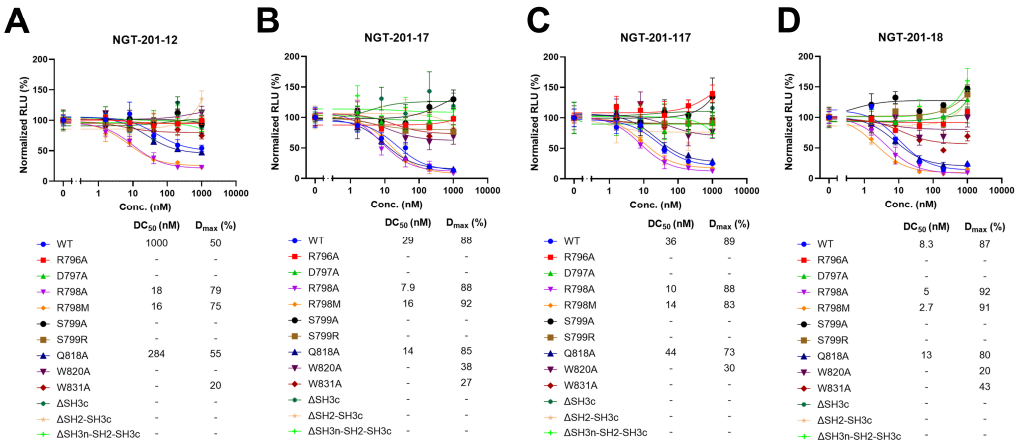

Figure S4. Dose-response curves showing the effect of NGT-201-12/17/117/18 on the degradation of wild-type (WT) nLuc-VAV1 and various point mutants within the predicted CRBN/NGT-201-12 interaction interface in HEK293T cells.

Data are presented as mean ± SD from three independent experiments. The table inset summarizes the DC_{50} and D_{max} values for each mutant.

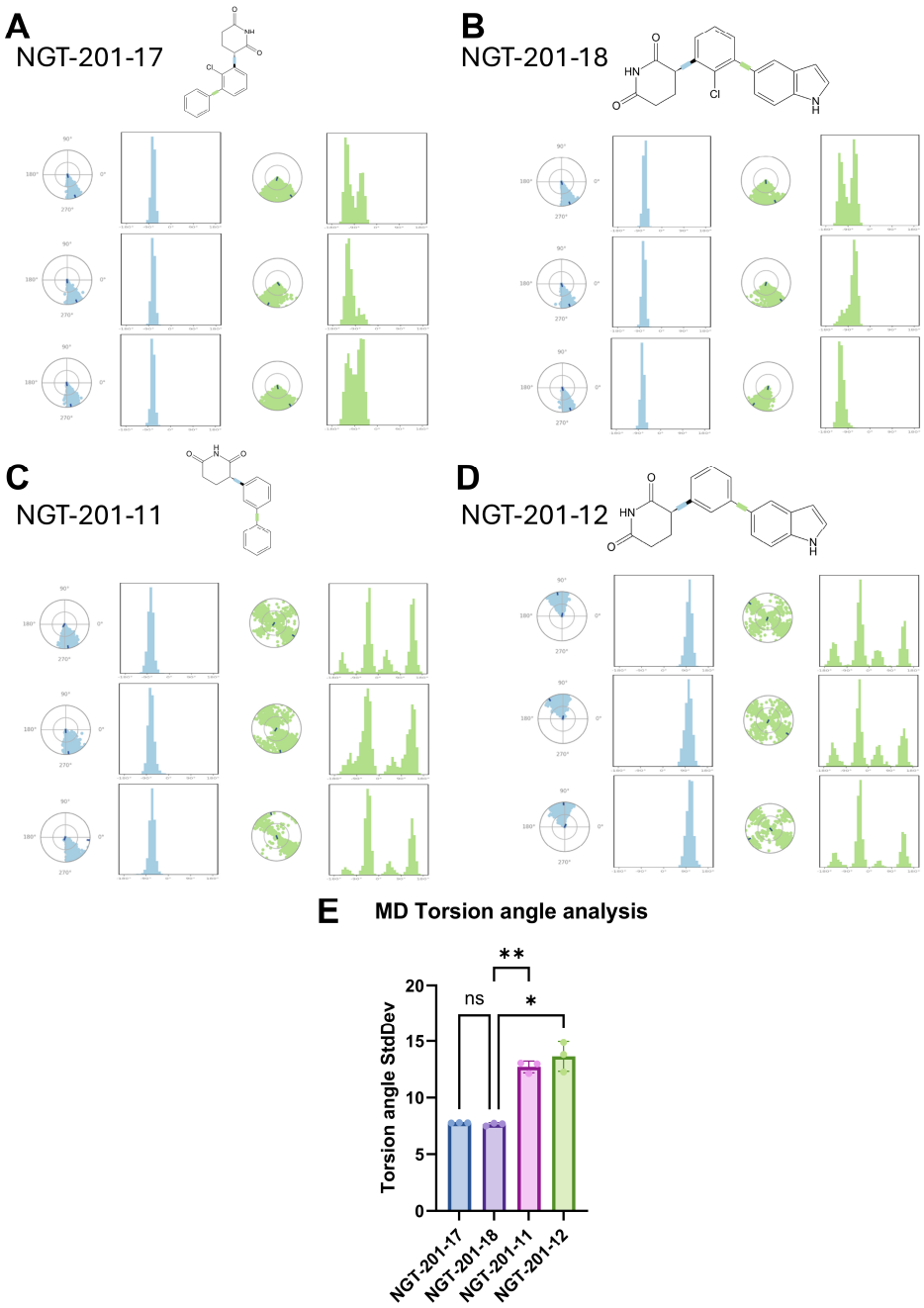

Figure S5. Ligand RMSF and torsion angle analysis of the 100ns molecular dynamics simulation trajectories (n=3) of selected compounds in the CRBN-glue binary model.

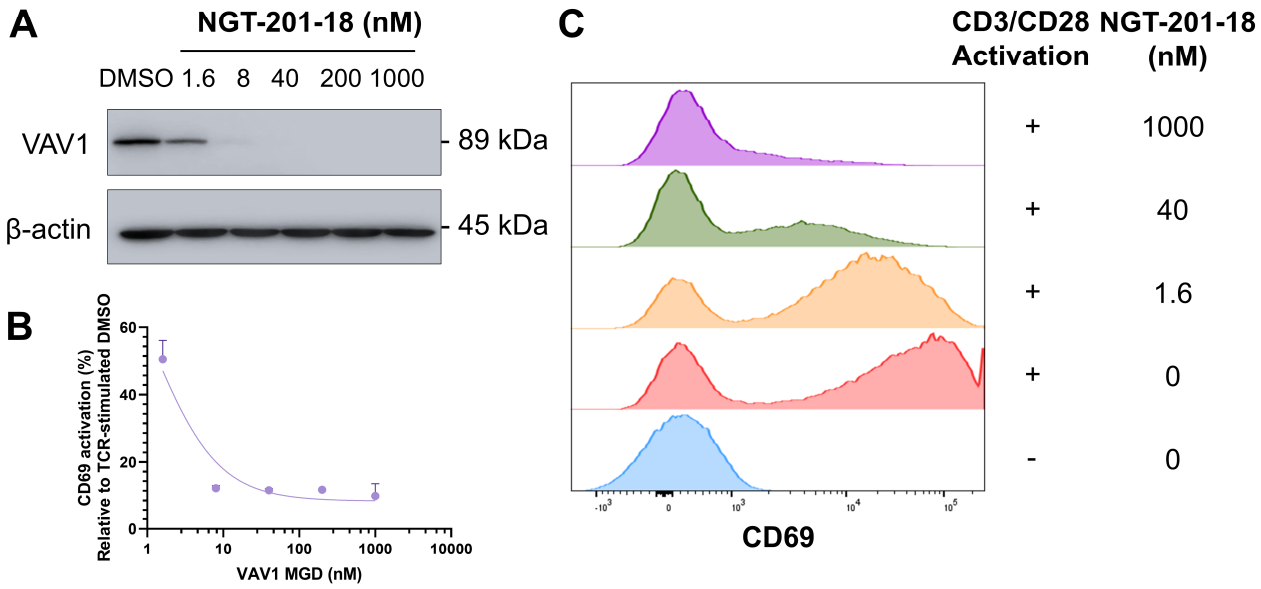

Figure S6. NGT-201-18 Induced VAV1 Degradation Inhibits Human T Cell Activation.

Primary human T cells were treated with a 5-point, 5-fold serial dilution of NGT-201-18 (starting concentration: 1000 nM) or DMSO control for 24 hours, followed by activation with anti-CD3/CD28 magnetic beads for an additional 12 hours. Cellular analyses were subsequently performed by Western blotting for VAV1 and flow cytometry for the activation marker CD69.(A) Western blot analysis confirming dose-dependent VAV1 degradation induced by NGT-201-18 in primary human T cells.(B) Quantification of T cell activation presented as the percentage of CD69 positive cells relative to the TCR-stimulated DMSO control. CD69 activation was calculated based on the Median Fluorescence Intensity (MFI). Data are presented as the mean±SD for n=3 biological replicates.(C) Representative flow cytometry histograms illustrating CD69 surface presentation on human T cells following the indicated treatments.

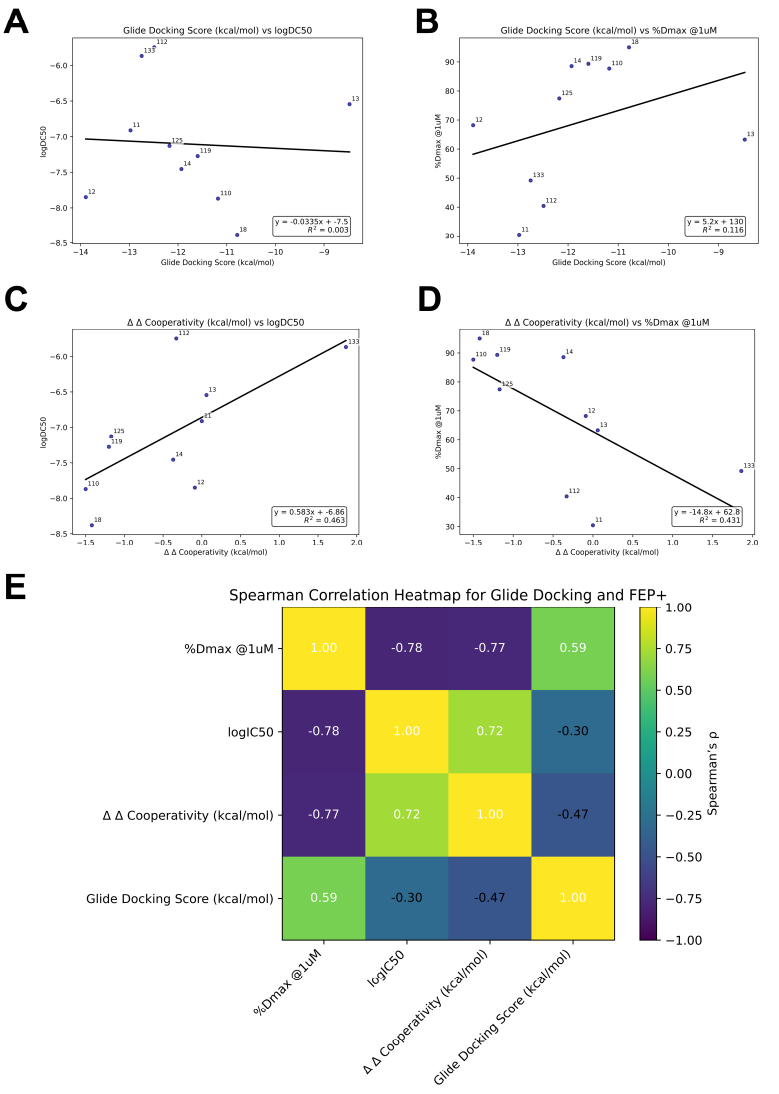

Figure S7. Correlation between FEP+ calculated $\Delta\Delta G^0_{coop}$ or Glide Docking Score and experimentally determined $logDC_{50}$ or $\%D_{max}$ at 1 μM.

(A) Pearson correlation between $\Delta\Delta G^0_{coop}$ and $logDC_{50}$. **(B)** Pearson correlation between $\Delta\Delta G^0_{coop}$ and $\%D_{max}$ at 1 μM. **(C)** Pearson correlation between Glide Docking score and $logDC_{50}$. **(D)** Pearson correlation between Glide Docking score and $\%D_{max}$ at 1uM. **(E)** Heatmap of Spearman correlation between FEP+ calculated $\Delta\Delta G^0_{coop}$ or Glide Docking Score and $logDC_{50}$ or $\%D_{max}$ at 1 μM.

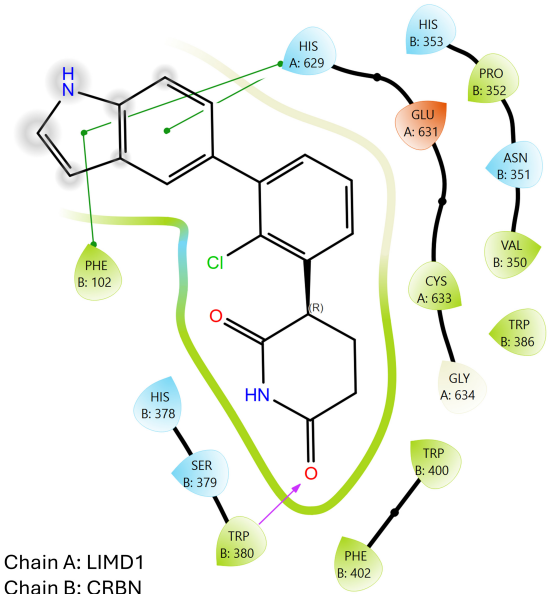

Figure S8. Protein ligand interaction diagram of CRBN:LIMD1:NGT-201-18 model

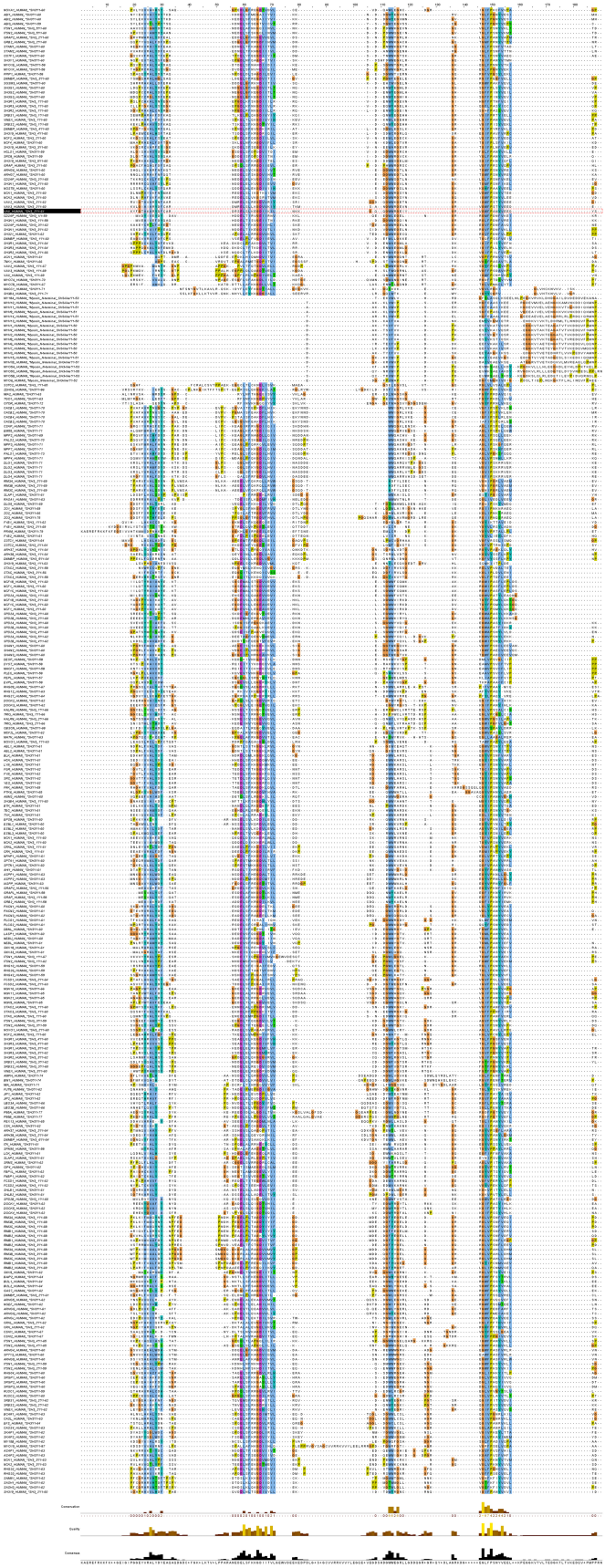

Figure S9. Human SH3 domain sequence alignment. VAV1 SH3_2 highlighted in red box.

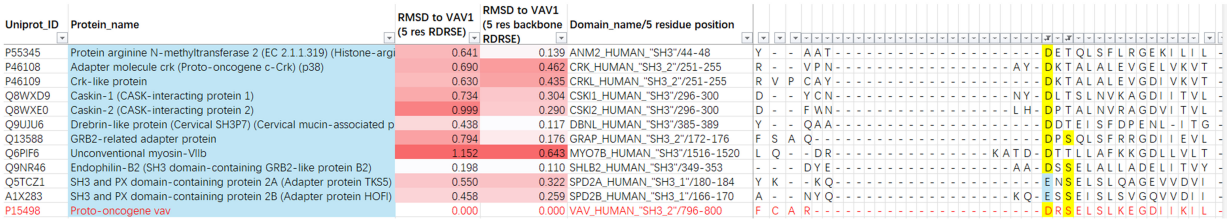

Uniprot_ID	Protein_name	RMSD to VAV1 (5 res RDRSE)	RMSD to VAV1 (5 res backbone RDRSE)	Domain_name/5 residue position
P55345	Protein arginine N-methyltransferase 2 (EC 2.1.1.319) (Histone-argi	0.641	0.139	ANM2_HUMAN_"SH3"/44-48
P46108	Adapter molecule crk (Proto-oncogene c-Crk) (p38)	0.690	0.462	CRK_HUMAN_"SH3_2"/251-255
P46109	Crk-like protein	0.630	0.435	CRKL_HUMAN_"SH3_2"/251-255
Q8WXD9	Caskin-1 (CASK-interacting protein 1)	0.734	0.304	CSKI1_HUMAN_"SH3"/296-300
Q8WXE0	Caskin-2 (CASK-interacting protein 2)	0.999	0.290	CSKI2_HUMAN_"SH3"/296-300
Q9UJU6	Drebrin-like protein (Cervical SH3P7) (Cervical mucin-associated p	0.438	0.117	DBNL_HUMAN_"SH3"/385-389
Q13588	GRB2-related adapter protein	0.794	0.176	GRAP_HUMAN_"SH3_2"/172-176
Q6PIF6	Unconventional myosin-VIIb	1.152	0.643	MYO7B_HUMAN_"SH3"/1516-1520
Q9NR46	Endophilin-B2 (SH3 domain-containing GRB2-like protein B2)	0.198	0.110	SHLB2_HUMAN_"SH3"/349-353
Q5TCZ1	SH3 and PX domain-containing protein 2A (Adapter protein TKS5)	0.550	0.322	SPD2A_HUMAN_"SH3_1"/180-184
A1X283	SH3 and PX domain-containing protein 2B (Adapter protein HOFI)	0.458	0.259	SPD2B_HUMAN_"SH3_1"/166-170
P15498	Proto-oncogene vav	0.000	0.000	VAV_HUMAN_"SH3_2"/796-800

Figure S10. SH3 domain sequence alignment and 5-residue (RDRSE) structural alignment with VAV1, showing the proteins with conserved D or E at 797 position and S or T at 799 position.

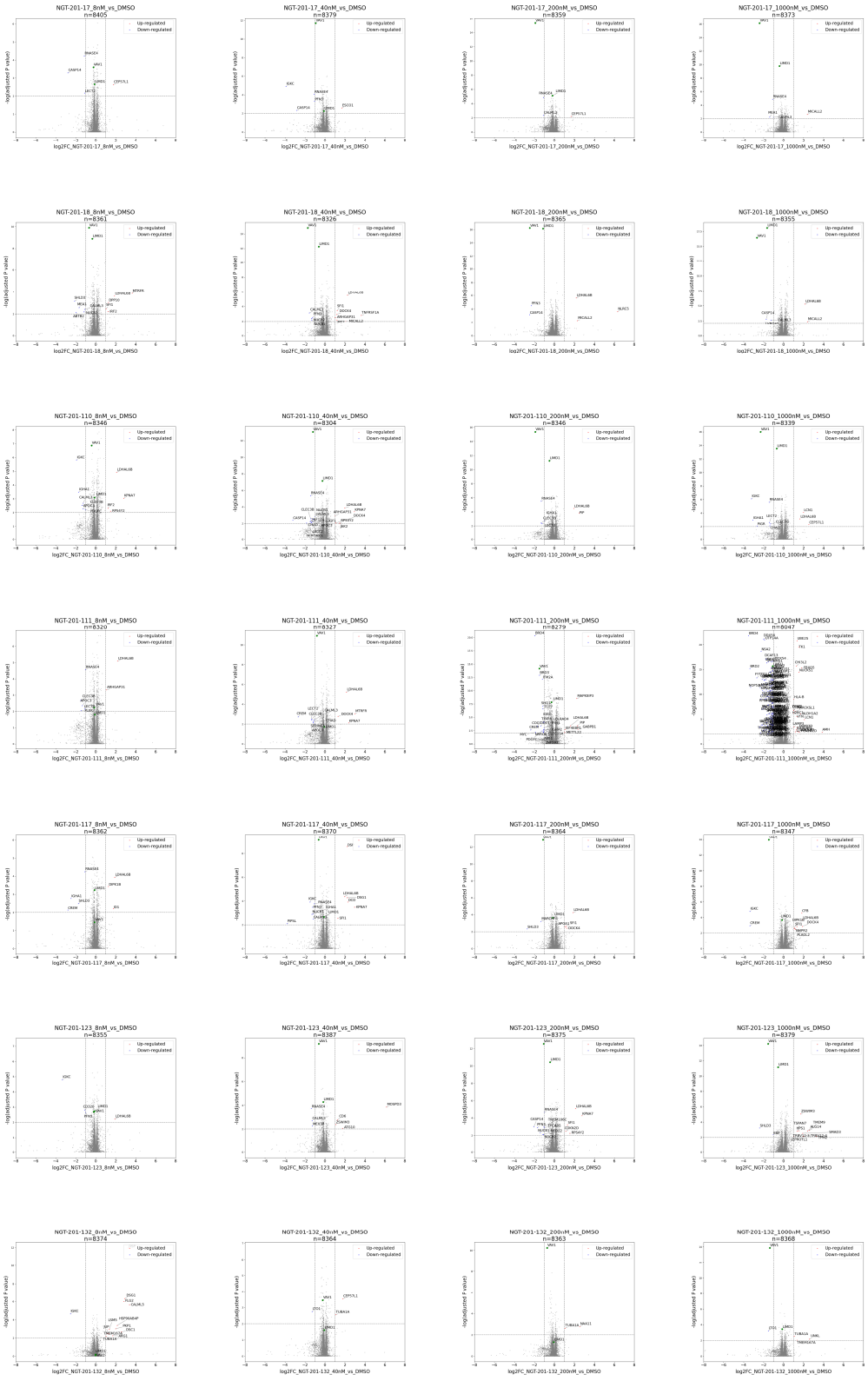

Figure S11. Volcano plots of NGT-201-17 to -132 associated with Figure 6.

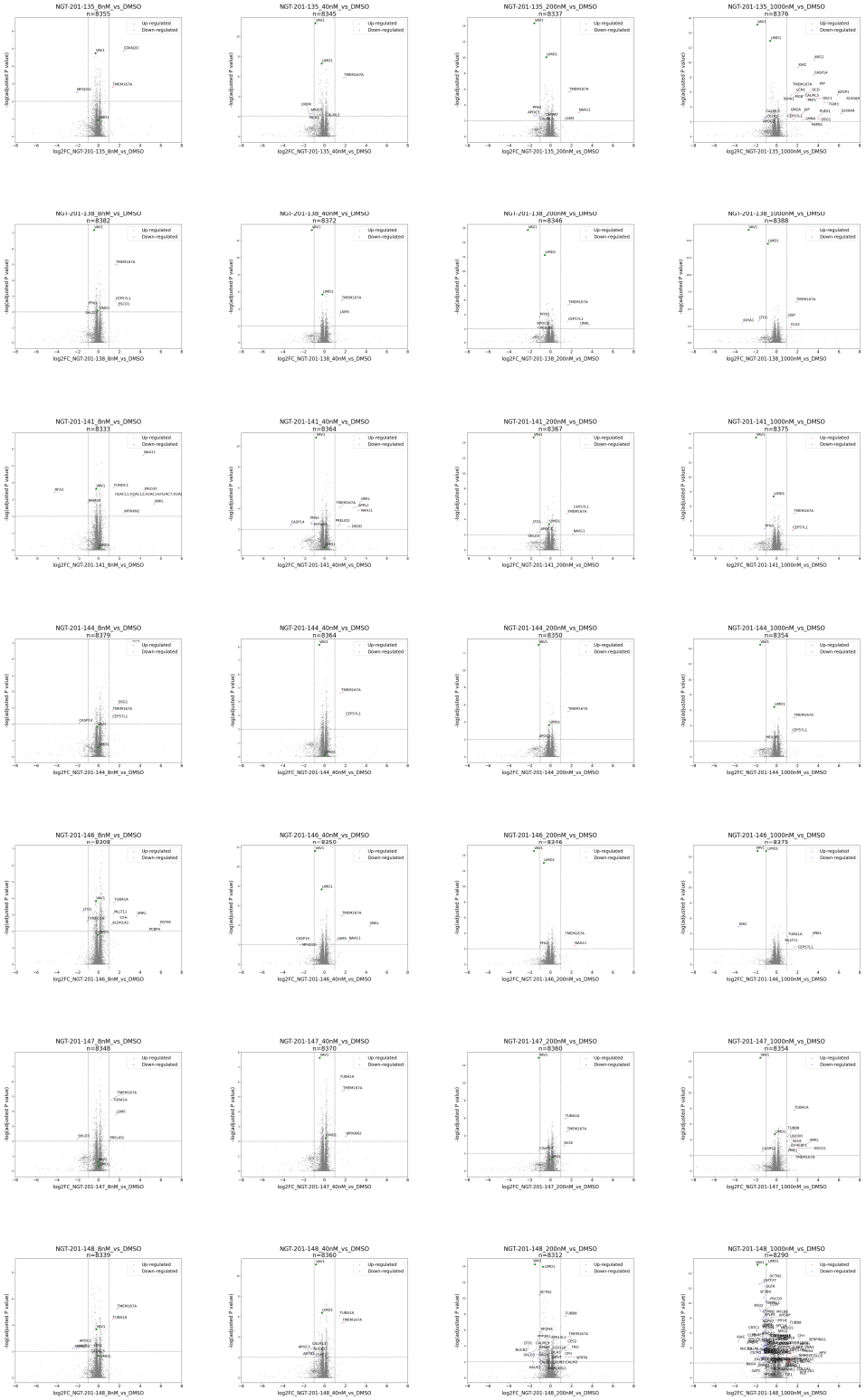

Figure S12. Volcano plots of NGT-201-135 to -148 associated with Figure 6.

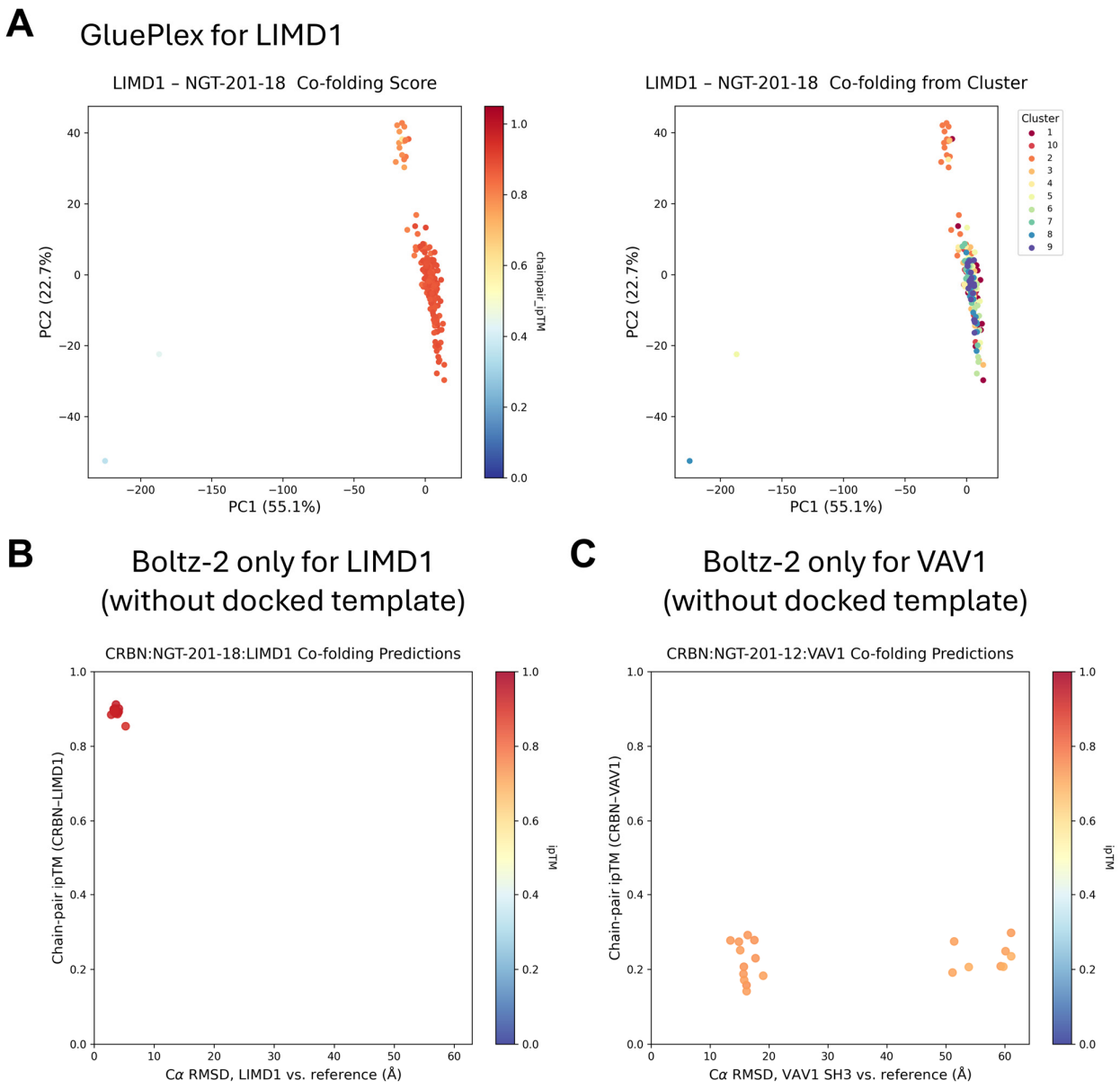

Figure S13. Benchmarking Boltz-2 performance with and without docking templates for canonical (LIMD1) versus non-canonical (VAV1) neosubstrates.

(A) Principal Component Analysis (PCA) of the co-folded structures generated by the full GluePlex pipeline for the LIMD1:NGT-201-18:CRBN complex, colored by chainpair_ipTM (left) or the original HADDOCK template cluster number (right). **(B)** Co-folding predictions for the LIMD1 ternary complex using Boltz-2 in isolation (without HADDOCK docking templates). The plot of chain-pair ipTM against Cα RMSD (relative to the alignment-based reference model) demonstrates that Boltz-2 can successfully predict canonical G-loop interactions *de novo*. **(C)** Co-folding predictions for the VAV1 ternary complex using Boltz-2 in isolation. The model completely fails to predict the novel RT-loop interface (yielding low ipTM and high RMSD) in the absence of the physics-based docking templates provided by the full GluePlex workflow. All Boltz-2 runs were performed with MSA generation disabled provided with individual protein templates.